Impact of Dual Calcium and Manganese Substitution of La-deficient perovskites on structural and related Catalytic Properties: Future opportunities in next Three-Way-Catalyst Generation?

Jianxiong Wu, Yuanshuang Zheng, Jean-Philippe Dacquin, Nora Djelal, Catherine Cordier, Christophe Dujardin, Pascal Granger

▶ **To cite this version:**

Jianxiong Wu, Yuanshuang Zheng, Jean-Philippe Dacquin, Nora Djelal, Catherine Cordier, et al.. Impact of Dual Calcium and Manganese Substitution of La-deficient perovskites on structural and related Catalytic Properties: Future opportunities in next Three-Way-Catalyst Generation?. Applied Catalysis A : General, 2021, Applied Catalysis A : General, 619, pp.118137. 10.1016/j.apcata.2021.118137 . hal-03213707

HAL Id: hal-03213707
https://hal.univ-lille.fr/hal-03213707

Submitted on 24 Apr 2023

HAL is a multi-disciplinary open access archive for the deposit and dissemination of scientific research documents, whether they are published or not. The documents may come from teaching and research institutions in France or abroad, or from public or private research centers.

L'archive ouverte pluridisciplinaire **HAL**, est destinée au dépôt et à la diffusion de documents scientifiques de niveau recherche, publiés ou non, émanant des établissements d'enseignement et de recherche français ou étrangers, des laboratoires publics ou privés.

Distributed under a Creative Commons Attribution - NonCommercial 4.0 International License

Version of Record: https://www.sciencedirect.com/science/article/pii/S0926860X21001514
Manuscript_cb664fa7e639e4d775e03fb8b787ba77

Submitted to a special issue in the journal Applied Catalysis A: General dedicated to the 65th anniversary of Professor Vasile I. Parvulescu
Revised manuscript ID : APCATA-D-21-00104

Impact of Dual Calcium and Manganese Substitution of La-deficient perovskites on structural and related Catalytic Properties : Future opportunities in next Three-Way-Catalyst Generation?

Jianxiong Wu[1], Yuanshuang Zheng[1], Jean-Philippe Dacquin[1], Nora Djelal[1], Catherine Cordier[2], Christophe Dujardin[1], Pascal Granger[1*]

[1] Univ. Lille, CNRS, Centrale Lille, Univ. Artois, UMR 8181 - UCCS - Unité de Catalyse et Chimie du Solide, F-59000 Lille, France
[2] Univ. Lille, CNRS, INRAE, Centrale Lille, UMR8207 – UMET - Unité Matériaux Et Transformations, F-59000 Lille, France

* Corresponding author : Email pascal.granger@univ-lille.fr
Phone number : +33 320 434 938

© 2021 published by Elsevier. This manuscript is made available under the CC BY NC user license
https://creativecommons.org/licenses/by-nc/4.0/

Abstract

The impact of La-deficiency and substitution by calcium and manganese in $LaFeO_3$ has been investigated in Three-Way-Catalysis. Despite significant structural distortions, predominantly induced by calcium substitution, no significant phase segregation occurs. On the other hand, bulk and surface characterization revealed the stabilization of Mn^{4+} and Fe^{4+} in different extent. Kinetic analysis of CO and propene oxidation reactions and the NO reduction reaction showed that $La_{0.7}Fe_{0.8}Mn_{0.2}O_3$ exhibits the best performance. By contrast, a detrimental effect of calcium more pronounced for propene oxidation is observed. It was found that catalytic properties are neither related to bulk properties nor to the extent of specific surface area but are mostly governed by the redox couple Mn^{4+}/Mn^{3+}. The formation of Fe^{4+} improving with partial substitution of La by Ca in A-site was not found as a determining criterion.

Keywords : Perovskite, Three-Way-Catalyst, La-deficient $La_{1-x}FeO_3$, Dual calcium manganese substitution, CO and propene oxidation, NO reduction.

1. Introduction

Perovskites (ABO_3) structures have been utilized in many oxidative catalytic applications and catalytic end-of-pipe technologies to treat atmospheric pollutants from Diesel exhaust, i.e. Diesel oxidation Catalysts, NO_x Storage Reduction catalysts [1-4]. Among the different compositions previously studied, stoichiometric $LaMnO_3$ [1,3] and none-stoichiometry La_xMnO_3 structures [5] attracted the interest of several investigators. As example, Chen et al. [5] reported improved performance for NO oxidation to NO_2 on $La_{0.9}MnO_3$ ascribed to higher formation of Mn^{4+}. These authors explained this gain in catalytic properties to the formation of more active oxygen species bonded to Mn^{4+}. The catalytic properties of $LaMn_{0.9}O_3$ were also examined for methane combustion with improved performances related to specific surface area enhancement jointly to higher density of defective sites [6]. Manganites have been extensively studied in oxidation reactions for light alkanes (C_2-C_7) and alkenes. [7,8].

The stabilization of Mn^{4+} instead of Mn^{3+} occurs even for stoichiometric $LaMnO_3$ composition. In that case, the excess of positive charges will be counterbalanced by an oxygen overstoichiometry. As reported elsewhere [9], perovskite structures can accommodate a wide variety of cations in B-site with mixed valency in case of non-stoichiometry of B or A cations or partial substitution with cations having different oxidation states. By way of illustration, Onrubia et al. [1] found that La^{3+} substitution by Sr^{2+} in Sr-doped $LaCoO_3$ induces the creation of oxygen vacancies with unchanged oxidation state for cobalt. On the other hand, these authors observed that the same substitution in Sr-doped $LaMnO_3$ preferentially leads to an increase of the oxidation state of manganese shifting to Mn^{4+}. For dual site substitutions, such as La^{3+} by Ca^{2+} in A-site and Co^{3+} by Mg^{2+} in B-site of parent $LaCoO_3$ material, a shift of the oxidation state of Co from +III to +IV is observed leading to a rate enhancement in toluene oxidation. Such gain in catalytic activity has been explained from a preferential suprafacial mechanism. rather than intrafacial mechanism [9].

Starting from stoichiometric $LaFeO_3$ and La-deficient $La_{0.7}FeO_3$ as benchmark compositions, single and dual substitution have been investigated in this study. Particular attention was paid to change in structural and electronic features induced by such substitutions which can lead to the stabilization of manganese or iron in unusual +IV oxidation state [10]. Accordingly, two redox couples, Fe^{4+}/Fe^{3+} and Mn^{4+}/Mn^{3+} can coexist and could influence the resulting catalytic properties. Leontiou et al. [11] found a greater stabilization of Fe^{4+} in Sr-doped $LaFeO_3$ from Mössbauer spectroscopy. These authors observed that the highest activity in NO reduction by CO was obtained on the perovskites having the lowest amount of Fe^{4+} and the highest amount of Fe^{3+}. Zhu and Thomas [12] reported that understanding the impact of B-site substitution on the overall performance is not trivial due to the coexistence of two redox systems which can be equally involved in NO decomposition. The identification of the most efficient redox couple remains empirical and is not formally related to a permanent oxidation state or the coexistence of different oxidation states [12].

Despite higher scarce examples, the potential interest of perovskites has been already tackled for three-way-catalysts but in simulated conditions which are often far from the typical compositions of the automotive exhaust gas. Previous investigations showed that $LaMnO_3$ catalyst can be a good candidate for CO [13] and hydrocarbon oxidation [14] as well as NO reduction [16-18]. Improved performance in NO reduction by propene have been reported on Cu-substituted $LaMnO_3$ perovskite in stoichiometric or slightly oxidizing conditions related to adsorbed ad-NO_x intermediates through the oxidation of NO by adsorbed oxygen species on anionic vacancies. On the other hand, a detrimental effect is observed with a rise in gaseous oxygen concentration because an excessive surface concentration of active oxygen species favors the preferential oxidation of propene [15-17].

Iron perovskites were selected as parent materials because of their improved thermal stability giving rise to better durability [18]. The impact of lanthanum substitution by calcium and iron

by manganese on the catalytic performance in three-way conditions has been investigated taking the occurrence of possible phase segregation into account that can improve/deteriorate activity and stability as well as modify the balance between reductive and oxidative properties [10].

2. Experimental

2.1. Catalyst preparation

Sol-gel method earlier described [19] was implemented for the preparation of parent and dual substituted perovskites according to a citrate route. Lanthanum, iron, manganese nitrate precursor salts were dissolved with citric acid (AC) in deionized water with CA/A+B =1. The solution thus obtained was subjected to evaporation in a rotary evaporator at 60°C with a rotating velocity of 30 rpm up to the formation of a gel. After drying in a static oven at 80°C for 48 h, the dried sample was calcined in air at 600°C for 8 h with a heating temperature dT/dt = 2°C/min.

2.2. Physicochemical characterization

X-ray diffraction (XRD) measurements were performed on a Bruker AXS D8 diffractometer (Cu Kα source, λ = 0.154 nm). XRD patterns were recorded in the 2θ range of 10-80 degree. Lattice parameters and unit cell volumes were adjusted from the Rietveld refinement method. Crystallite size was estimated by the Williamson-Hall approach. Standard deviations were calculated by Bérar correction.

Ex situ Mössbauer spectra were recorded at room temperature using a ^{57}Co (Rh) source. Lorentzian shape peaks were assumed for data fitting. Pure iron foil was used as reference for the calculation of hyperfine field (HF), isomer shift (IS) and quadrupole splitting (QS).

Scanning Electron Microscopy (SEM) micrographs were recorded on a Hitachi S-4700 Cold Field Emission Gun Scanning Electron Microscope operating at an acceleration voltage of 15 kV. Energy-dispersive X-ray spectroscopy (EDS) was used for elemental analysis. Oxford EDS system was employed for these analyzes. The volume probed by this technique was 1 μm^3.

H_2-Temperature-Programmed Reduction (H_2-TPR) experiments were carried out on a Micromeritics AutoChem 2920 analyzer. 50 mg samples, subjected to 50 mL/min flowrate of 5 vol.% H_2 in Ar, were heated to 1000°C with a heating rate of 5 °C/min. Hydrogen consumption was controlled by a thermal conductivity detector. O_2-Temperature-Programmed-Desorption (O_2-TPD) experiments were performed on the same apparatus with the same mass of catalyst. The sample was heated under He up to 1000°C with dT/dt = 10 °C/min. Oxygen concentration in the gas phase released from the catalyst surface during the ramp of temperature was measured by gas chromatography and mass spectrometery (m/z = 32). Prior to O_2-TPD experiments, the samples were systematically pre-heated in pure oxygen at 600°C for 1 h.

Porosity measurements on a Micromeritics Tristar analyzer were carried out -196°C. Prior to nitrogen physisorption, the samples were outgassed under vacuum for 4 h. Specific surface area (SSA) was determined according to Brunauer-Emmett-Teller (BET) theory, while the Barret-Joyner-Halenda (BJH) theory led to pore size distribution.

X-ray photoelectron spectra were recorded on a Kratos Axis Ultra spectrometer equiped with a monochromatized Al Kα source. Binding Energy (B.E.) values were corrected compared to

the C1s core level set at 284.8 eV. Casa XPS software was used for spectral decomposition accounting for mixed Gaussian/Lorentzian (70/30) line profile.

2.3. Catalytic measurements

Temperature-Programmed-Reaction experiments (TPR) were performed at atmospheric pressure according to the same protocol described elsewhere [10]. A fixed bed flow reactor was fed with 200 mg catalysts, with average grain size of 150 μm, mixed with the same mass of SiC. The total inlet volumetric flowrate (Q_0) at 12 L h^{-1}, corresponded to Q_0/W of 60,000 mL h^{-1} g^{-1}. The protocol depicted in Fig. S1 in Supplementary Information (SI) included 4 successive TPR experiments performed in stoichiometric, lean and rich conditions with gas mixture compositions in Table S1 in SI. The outlet NO, NO_2, N_2, N_2O, O_2, H_2, CO, C_3H_6 and C_3H_8 concentrations were controlled by a Thermo Scientific Model 42i-HL chemiluminescence NO_x analyzer and an Agilent 490 Micro Gas Chromatography. Rate calculations were detailed in SI assuming the mass balance equation of a plug flow reactor in agreement with Eqs. (S1)-(S3) in SI. Preliminary verifications showed that mass transfer limitations should not occur significantly for conversion lower than 0.4 in agreement with the boundary conditions given by Eq. (S4) in SI.

3. Results and discussion

3.1. Induced effect of single and dual calcium manganese substitutions on structural features of parent $LaFeO_3$ and $La_{0.7}FeO_3$ perovskites

The elemental analysis confirms the chemical compositions for the parent $LaFeO_3$, $LaMnO_3$ and $La_{0.7}FeO_3$ perovskites as well as for the $La_{0.7}Fe_{0.8}Mn_{0.2}O_3$ and $La_{0.6}Ca_xFe_{0.8}Mn_{0.2}O_3$ perovskites (see Table S2 in SI).

3.1.1. XRD analysis

Fig. 1 shows X-ray diffractograms recorded on single and dual substituted stoichiometric and La-deficient parent perovskites. An orthorhombic perovskite structure is usually characterized with the space group Pnma (PDF 37-1493). The lack of detection of extra reflections emphasizes the absence of significant phases segregations. Minor shift in 2θ values is observed on the most intense (002) reflection on XRD pattern recorded on $La_{0.7}Fe_{0.8}Mn_{0.2}O_3$ consistent with a slight contraction effect of the unit cell as reported in Table 1. In principle, the substitution of Fe^{3+} by Mn^{3+} should not induce discernible changes on the unit cell because they have comparable ionic radii. By contrast, such effect could be assigned to partial stabilization of Fe^{4+} and/or Mn^{4+} characterized by lower ionic radii of respectively 0.585 and 0.56 Å vs. 0.64 Å for Fe^{3+} and 0.66 Å for Mn^{3+}.

The absence of MnO_x and CaO bulk detectable impurities is also remarkable on dual substituted perovskites (see Fig. 1(B)) emphasizing the fact that Ca^{2+} and Mn^{3+} would be predominantly stabilized in the perovskite lattice. Slight contraction effects are noticeable on La-deficient $La_{0.7}Ca_xFe_{0.8}Mn_{0.2}O_3$ compositions which accentuate on the stoichiometric $La_{0.6}Ca_{0.4}Fe_{0.8}Mn_{0.2}O_3$ composition (see Table 1) underlining sharp structural deformations on the stoichiometric composition. Although the topology of substituted perovskites is thermodynamically stable, the structure may distort as a result of preferential bonding of A and B cations [20,21]. Typically, the formation of π(B-O) in $A_yA_{1-y}B_xB_{1-x}O_3$ can compete with σ(A-O). This competition may also concern σ(B-O) and σ(B'-O) bond formation which means that the covalency of the B-O bond will depend on the nature of the B' and A cations

[22,23]. In general, BO_6 octahedra tilting, bond length change, cationic displacements and anionic vacancies are the main parameters which govern structural deformation of substituted perovskites. The substitution of La^{3+} by Ca^{2+} creates electronic imbalances, while the comparison of their ionic radii (1.36 Å vs. 1.34 Å respectively) should not induce structural changes. Based on this, charge imbalances should be compensated through the creation of anionic vacancies and/or through changes in the valence state of B cation. As aforementioned, the electroneutrality could induce the stabilization of Fe^{4+} and/or Mn^{4+} and would reasonably explain the contraction effects observed on La-deficient compositions and more importantly on the stoichiometric $La_{0.6}Ca_{0.4}Fe_{0.8}Mn_{0.2}O_3$ composition.

Table 1. Changes in structural features from XRD measurements induced by single and dual substitutions of parent stoichiometric $LaFeO_3$ and La-deficient $La_{0.7}FeO_3$ perovskites.

Catalysts	Crystal system	a(Å) [a]	b(Å) [a]	c(Å) [a]	unit cell volume(Å^3) [a]	Crystallite size (nm) [b]
$LaFeO_3$	orthorhombic	5.560(1)	7.861(0)	5.557(1)	242.88±0.05	29.4
$La_{0.7}FeO_3$	orthorhombic	5.560(0)	7.878(1)	5.535(1)	242.44±0.03	21.7
$La_{0.7}Fe_{0.8}Mn_{0.2}O_3$	orthorhombic	5.547(0)	7.815(0)	5.536(1)	240.07±0.01	20.4
$La_{0.6}Ca_{0.1}Fe_{0.8}Mn_{0.2}O_3$	orthorhombic	5.532(1)	7.801(0)	5.519(0)	238.22±0.06	24.8
$La_{0.6}Ca_{0.2}Fe_{0.8}Mn_{0.2}O_3$	orthorhombic	5.540(0)	7.773(1)	5.513(0)	237.46±0.03	23.7
$La_{0.6}Ca_{0.4}Fe_{0.8}Mn_{0.2}O_3$	orthorhombic	5.491(0)	7.764(1)	5.483(0)	233.78±0.05	21.3

[a] lattice parameters calculated from Rietveld refinement method
[b] crystallite size calculated by the Williamson-Hall plot method using LaB_6 as standard specimen

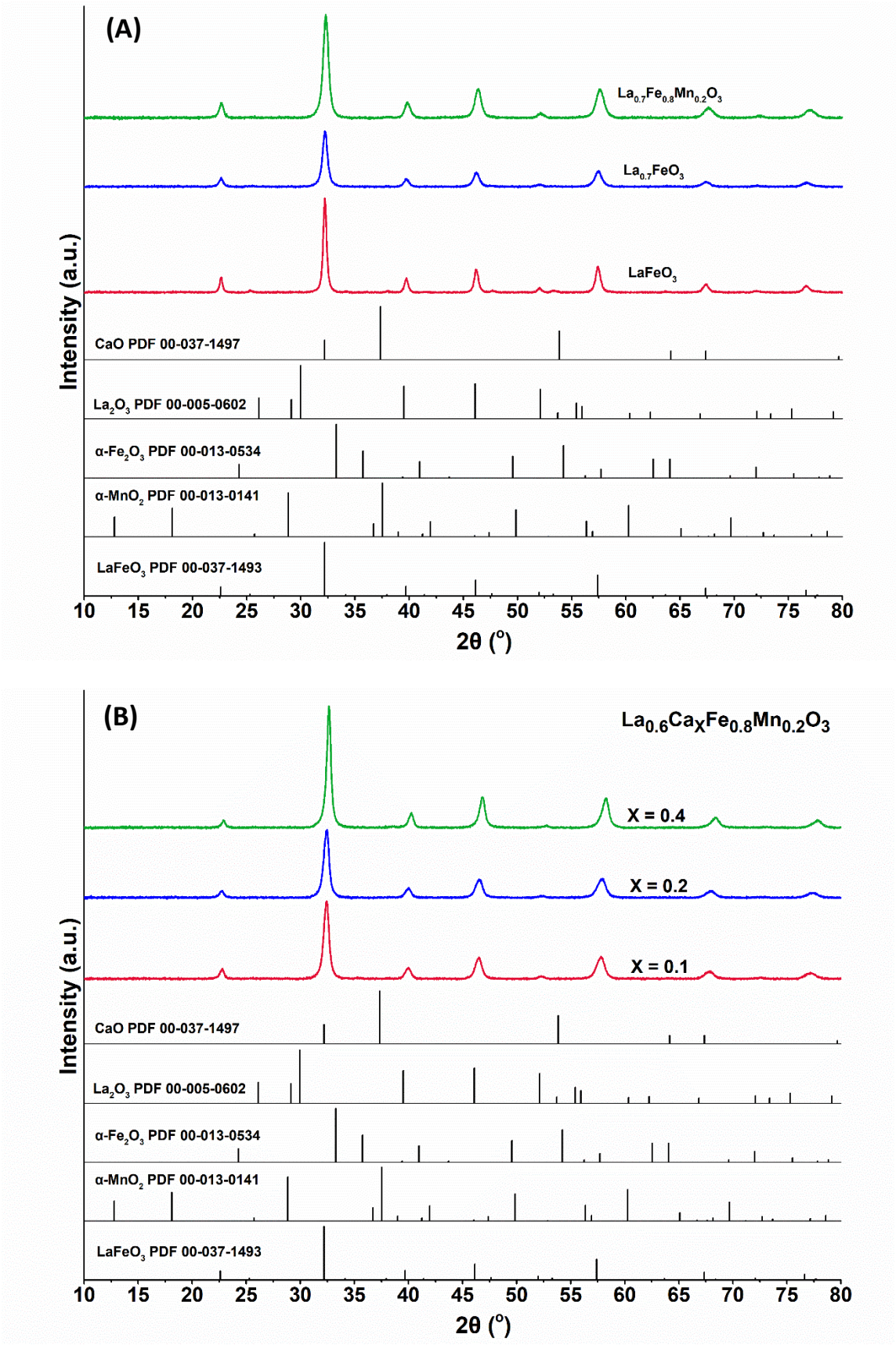

Fig. 1. XRD diffractograms of $LaFeO_3$, La-deficient $La_{0.7}Fe_{1-y}Mn_yO_3$ perovskites with $y = 0$ or 0.2 (A), and dual substituted $La_{0.6}Ca_xFe_{0.8}Mn_{0.2}O_3$ perovskites with $x = 0.1$, 0.2 or 0.4 (B).

3.1.2. Mössbauer spectroscopy

Mössbauer spectra, recorded at room temperature on parent and doped perovskites, are reported in Fig. S2 in SI. Spectra recorded on parent $LaFeO_3$ and $La_{0.7}FeO_3$ perovskites are featured by a predominant sextet [24,25] characteristic of cationic Fe^{3+} species in octahedral coordination surrounded by six O^{2-} ions whereas La^{3+} ions occupy eight corners of the orthorhombic unit cell along with a less intense paramagnetic singlet. Distortion of BO_6 octahedra from the ideal cubic structure was confirmed by the quadruple splitting. A visible broadening of line width appears for the Mn-doped perovskites along with marked quadruple splitting measuring the electrical field gradient at the iron site. Such phenomenon is ascribed to local environment effects that lead to anisotropic deformations of the environment of the Fe (+III) species in distorted octahedral sites [26]. Data fitting consisted in the superimposition of several sextets assigned to specific locations of cationic iron species. The contribution of quadrupole-split doublet, with the hyperfine parameters typical of super-paramagnetic magnetite particles has been taken into account for manganese substituted perovskite compositions [27,28]. The estimates of the Isomer Shift (IS), the Quadrupole Splitting (QS) and the Hyperfine magnetic Field (HF), fitted from Mössbauer spectra in Fig. S2 in SI, are collected in Table 2. They inform on the nature and coordination geometry of cationic iron species, electronic density and magnetic state. Their relative abundances have been calculated according to a binomial distribution [29]. For Mn-substituted perovskites, the component with high hyperfine field values has been assigned to Fe^{3+} involved in the electron delocalization process in the absence of manganese as nearest neighbors whereas lower HF values correspond to iron species surrounded by manganese. As a general trend, iron preferentially occupies octahedral sites. Nevertheless, significant deviations are remarkable on the distribution between A- and B-sites on $La_{0.6}Ca_{0.2}Fe_{0.8}Mn_{0.2}O_3$ characterized by balanced occupancy ratio of octahedral and tetrahedral sites. Battle et al. [30] reported in

orthorhombic type perovskite structure that the transition from cubic to orthorhombic structure results from an ordered arrangement of oxygen vacancies along [101] axes with layers of iron cations in tetrahedral coordination. Mere A site deficiency did not incur unusual oxidation state of iron species, indicating a charge compensation likely governed by the formation of oxygen vacancies. The presence of high spin Fe^{4+} species seems more related to incorporation of A site cations with lower valence regardless of stoichiometry or deficiency in A site. Isomer shift (IS) values which are characteristic of Fe (+III) species located in the octahedron sites increased with the amount of calcium doping implying that local distortion of octahedron is associated closely with cation doping in A site. This seems in agreement with XRD results that more calcium-doping causes remarkable asymmetry of the crystal structure especially for the stoichiometric $La_{0.6}Ca_{0.4}Fe_{0.8}Mn_{0.2}O_3$ composition.

Table 2. Hyperfine parameters from Mössbauer spectroscopy analysis of dual substituted $LaFeO_3$ and La-deficient $La_{0.7}FeO_3$ perovskites

Catalyst	Iron species	Coordination geometry	Phase/iron site [a]	Valency	HF (T) ± 0.1T	IS (mm/s) ± 0.05 mm/s	QS (mm/s) ± 0.05 mm/s	Relative abundance (%)
$LaFeO_3$	Fe^{3+}	Undistorted octahedron		2.8	55.0	0.57	-0.41	4.83
				3.29	51.9	0.37	-0.04	61.71
				3.35	48.1	0.32	-0.33	5.34
				2.7	47.7	0.58	0	6.68
	Fe^{3+}	Distorted octahedron		3.4	-	0.30	0.38	11.35
	$Fe^{3+\delta}$	Tetrahedron		3.8	-	0.14	0.16	5.26
	Fe^{4+}	High spin		4	37.0	0.07	-0.32	4.83
$La_{0.7}FeO_3$	Fe^{3+}	Undistorted octahedron		3.20	51.6	0.37	-0.01	52.35
				3.30	49.8	0.34	-0.02	13.87
				3.20	48.7	0.38	0.13	4.10
				3.00	46.3	0.48	0.02	7.40
	Fe^{3+}	Distorted octahedron		3.05	42.2	0.45	0.07	5.04
				3.00	18.9	0.48	-0.02	4.78
				3.10	16.0	0.44	0.02	4.77
				3.00	-	0.47	0.78	3.10
				3.30	-	0.35	0.32	2.48
	$Fe^{3+\delta}$	Tetrahedron		3.80	-	0.13	0.38	2.11
$La_{0.7}Fe_{0.8}Mn_{0.2}O_3$	Fe^{3+}	Octahedron	Fe_2O_3 or ferrihydrite		51.1	0.37	-0.03	19.58
	Fe^{3+}	Tetrahedron	$(Fe,Mn)_3O_4$-A or αFeOOH		48.1	0.40	-0.02	12.83
	Fe^{3+} and Fe^{2+}	Octahedron	$(Fe,Mn)_3O_4$-B		46.1	0.39	0.02	14.38
	Fe^{3+} and Fe^{2+}	Octahedron	$(Fe,Mn)_3O_4$-B		43.5	0.43	0.02	9.60
	Fe^{3+} and Fe^{2+}	Octahedron	$(Fe,Mn)_3O_4$-B		42.8	0.23	0.10	7.85
	Fe^{3+} and Fe^{2+}	Octahedron	$(Fe,Mn)_3O_4$-B		40.0	0.46	-0.06	11.00
	Fe^{3+}		Goethite aFeOOH		36.3	0.43	-0.05	9.44
	Fe^{3+} and Fe^{4+}		α(Fe,Mn)OOH		32.9	0.33	0.11	2.31
	Fe^{3+}		O-Fe_2C or α(Fe,Mn)OOH		15.2	0.30	-0.02	6.04
	Fe^{3+}	Distorted octehedron	γ-FeOOH		-	0.45	0.57	2.81
	Fe^{3+}	Tetrahedron			-	0.19	0.33	3.40
	Fe^{3+}		ferrihydrite		-	0.61	0.24	0.76
$La_{0.6}Ca_{0.1}Fe_{0.8}Mn_{0.2}O_3$	Fe^{3+}		Fe_2O_3 or ferrihydrite		51.4	0.35	-0.03	18.14
	Fe^{3+}	Tetrahedron	Fe_3O_4-A		49.8	0.34	0.00	14.13
	Fe^{3+}	Tetrahedron	$(Fe,Mn)_3O_4$-A or αFeOOH		47.6	0.36	-0.01	13.35
	Fe^{3+} and Fe^{2+}	Octahedron	$(Fe,Mn)_3O_4$-B		45.2	0.43	-0.09	11.59
	Fe^{3+} and Fe^{2+}	Octahedron	$(Fe,Mn)_3O_4$-B		42.4	0.18	0.17	8.94
	Fe^{3+} and Fe^{2+}	Octahedron	$(Fe,Mn)_3O_4$-B		39.3	0.48	-0.09	8.08
	Fe^{3+}		Goethite αFeOOH		36.5	0.32	0.02	4.58
	Fe^{3+} and Fe^{4+}		α(Fe,Mn)OOH		33.8	0.33	0.11	4.16
	Fe^{3+}		O-Fe_2C or α(Fe,Mn)OOH		12.6	0.42	-0.15	5.95
	Fe^{3+}	Distorted octahedron	None magnetic oxide		-	0.28	0.84	5.15
	Fe^{3+}		ferrihydrite		-	0.61	0.24	0.64
	Fe^{3+}	Distorted octahedron			-	0.42	0.00	1.30
	Fe^{4+}		High spin		-	0.05	0.00	3.99

$La_{0.6}Ca_{0.2}Fe_{0.8}Mn_{0.2}O_3$	Fe^{3+}	Tetrahedron	Fe_3O_4-A	49.9	0.25	-0.06	9.29
	Fe^{3+}	Tetrahedron	$(Fe,Mn)_3O_4$-A or αFeOOH	49.0	0.48	0.03	18.95
	Fe^{3+}	Tetrahedron	$(Fe,Mn)_3O_4$-A or αFeOOH	48.6	0.17	-0.06	12.87
	Fe^{3+} and Fe^{2+}	Octahedron	$(Fe,Mn)_3O_4$-B	45.1	0.42	-0.04	15.24
	Fe^{3+} and Fe^{2+}	Octahedron	$(Fe,Mn)_3O_4$-B	42.1	0.27	0.09	13.00
	Fe^{3+} and Fe^{2+}	Octahedron	$(Fe,Mn)_3O_4$-B	39.1	0.42	-0.06	9.20
	Fe^{3+}		Goethite αFeOOH	34.6	0.58	0.00	6.43
	Fe^{3+} and Fe^{4+}		α(Fe,Mn)OOH	34.4	-0.19	0.26	3.65
	Fe^{3+}	Distorted octahedron	Fe^{3+} none metallic oxide	-	0.41	0.93	4.19
	Fe^{4+}		Fe^{4+} hsp	-	-0.01	0.72	3.35
	Fe^{3+}	Distorted octahedron	γ-FeOOH or Fe^{3+}	-	0.35	0.59	3.83
$La_{0.6}Ca_{0.4}Fe_{0.8}Mn_{0.2}O_3$	Fe^{3+}	Tetrahedron	Fe_3O_4-A	49.6	0.34	-0.04	8.65
	Fe^{3+}	Tetrahedron	$(Fe,Mn)_3O_4$-A or αFeOOH	47.0	0.34	-0.03	16.29
	Fe^{3+} and Fe^{2+}	Octahedron	$(Fe,Mn)_3O_4$-B	44.3	0.33	-0.01	14.28
	Fe^{3+} and Fe^{2+}	Octahedron	$(Fe,Mn)_3O_4$-B	41.9	0.36	-0.03	13.52
	Fe^{3+} and Fe^{2+}	Octahedron	$(Fe,Mn)_3O_4$-B	39.6	0.34	-0.01	11.11
	Fe^{3+}		Goethite αFeOOH	36.3	0.42	-0.04	11.18
	Fe^{3+} and Fe^{4+}		α(Fe,Mn)OOH	32.6	0.39	-0.07	8.34
	Fe^{3+}		O-Fe_2C ou α(Fe,Mn)OOH	14.2	0.38	0.08	8.74
	Fe^{3+}	Tetrahedron		-	0.26	0.76	1.24
	Fe^{3+}	Tetrahedron		-	0.25	0.31	3.25
	Fe^{3+}		ferrihydrite	-	0.61	0.24	0.68
	Fe^{4+}			-	0.09	0.24	2.72

[a] -A and -B correspond to two distinct coordination sites for iron in magnetite

3.1.3. Scanning Electron Microscopy (SEM) coupled with Energy-dispersive X-ray spectroscopy (EDS).

SEM images recorded on single and dual substituted stoichiometric and La-deficient perovskite materials are illustrated in Fig. S3 in SI. Fig. 2 reports SEM analysis on $La_{0.7}Fe_{0.8}Mn_{0.2}O_3$ as example. Similar observations appear whatever the elemental composition. Large aggregates as well as absence of morphological organization is noticeable. Elemental compositions on the volume analyzed from Dispersive X-ray Spectroscopy analysis (1 μm^3) are reported in Table 3. The comparison of the atomic compositions thus obtained with those obtained from ICP-AES analysis (see Table S2 in SI) does not underline significant deviations. This comparison seems to indicate a random distribution of the elements in the volume analyzed. Back scattered electron images reveal no obvious disparity

for calcium and manganese. The same trend is observed on stoichiometric $LaFeO_3$, $La_{0.7}FeO_3$ and $LaMnO_3$ perovskites (Fig. S3(A)-(C) in SI). The absence of large spots that would reflect the formation of large aggregates irrespective of the composition agree with a preferential formation of a single perovskite phase. This confirms a predominant substitution of lanthanum by calcium and iron by manganese inside the perovskite lattice rather than formation of extra-lattice single metal oxides dispersed on the perovskite substrate. All these observations match with those obtained from XRD analyses which did not indicate discernible bulk impurities formation ascribed to manganese oxide segregation.

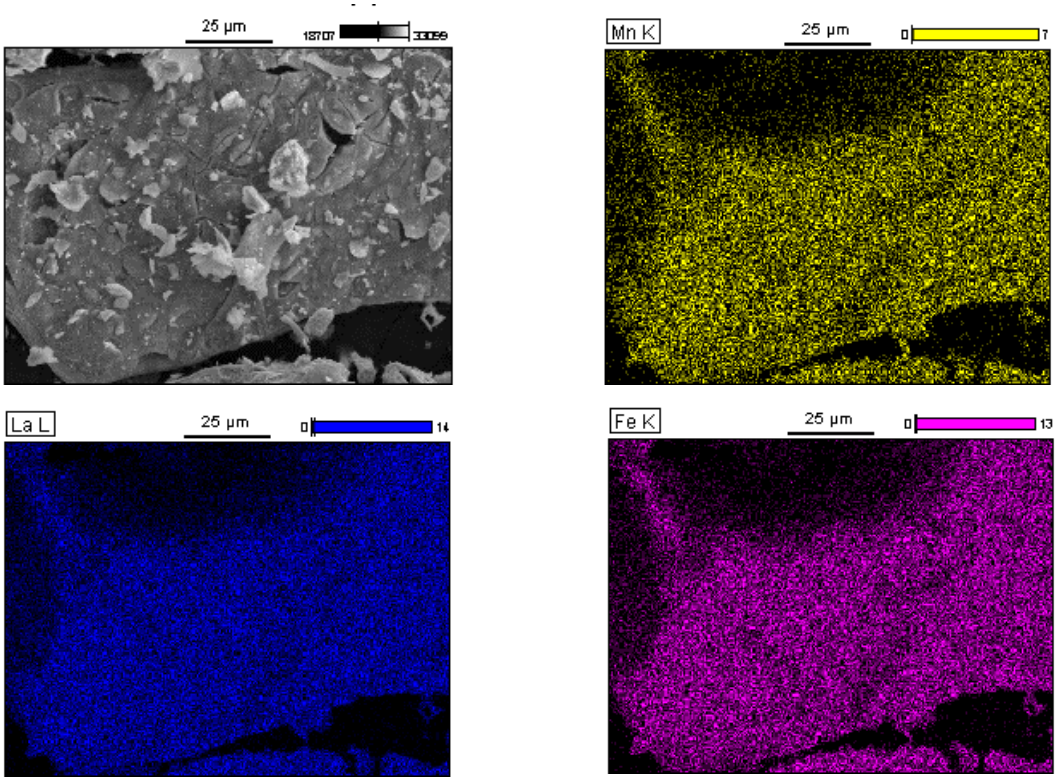

Fig. 2. SEM image and elemental mapping on $La_{0.7}Fe_{0.8}Mn_{0.2}O_3$ composition.

Table 3. Atomic composition from EDS analysis perovskite samples.

catalyst	Atomic composition (at.%)				Atomic ratio [a]	
	La	Ca	Fe	Mn	Mn/Fe	A/B
$LaFeO_3$	48.6	-	51.4	-		0.94 (1.02)
$La_{0.7}FeO_3$	38.0	-	62.0	-		0.61 (0.67)
$La_{0.7}Fe_{0.8}Mn_{0.2}O_3$	37.2	-	49.3	13.5	0.40 (0.40)	0.59 (0.71)
$La_{0.6}Ca_{0.1}Fe_{0.8}Mn_{0.2}O_3$	31.1	6.4	48.5	13.9	0.29 (0.25)	0.60 (0.68)
$La_{0.6}Ca_{0.2}Fe_{0.8}Mn_{0.2}O_3$	29.6	11.3	46.0	13.1	0.28 (0.15)	0.69 (0.78)
$La_{0.6}Ca_{0.4}Fe_{0.8}Mn_{0.2}O_3$	26.3	20.9	40.9	11.9	0.29 (0.25)	0.90 (1.00)

[a] calculated from ICP-AES in bracket

3.2. Reducibility and oxygen mobility

3.2.1. Hydrogen Temperature-Programmed Reduction (H_2-TPR) experiments

First experiments on benchmark $LaFeO_3$, $La_{0.7}FeO_3$ and $LaMnO_3$ (see Fig. 3(A)) revealed for $LaFeO_3$ a weak H_2 consumption below 700°C emphasizing unreducible sample in this temperature range. By contrast, two distinct H_2 consumptions on $La_{0.7}FeO_3$ take place in the temperature ranges 150-425°C and 425-625°C assigned to a two steps reduction of extra-framework hematite species: $Fe^{3+} \rightarrow Fe^{2+}$ and $Fe^{2+} \rightarrow Fe^{0}$. For the benchmark $LaMnO_3$, the H/Mn ratio agrees with the stabilization of Mn^{4+} characterized by a two steps reduction process of Mn^{4+} to Mn^{3+} and Mn^{3+} to Mn^{2+} respectively in the temperature ranges 250-500°C and above 650°C. This result emphasizes on this sample a current over-stoichiometry of oxygen which agrees with a classical formulae $LaMnO_{3+\delta}$. These preliminary experiments on benchmark catalysts reveal significant overlapping between the reduction of oxidic manganese and iron species which unfortunately cannot lead to accurate calculations neither on the atomic H/Mn and H/Fe ratios nor on the over-stoichiometry of oxygen. Hence, the estimates of the overall H/Mn+Fe have been calculated and the corresponding values are reported in Table 4. The reduction of extra-framework hematite species proceeds on

$La_{0.7}Fe_{0.8}Mn_{0.2}O_3$ similarly to $La_{0.7}FeO_3$. A discernible broad and weak shoulder arises above 600°C which reflects the reduction of Mn^{3+} to Mn^{2+}. On the basis of this information, the substitution of Fe^{3+} by Mn^{3+} in $La_{0.7}FeO_3$ did not suppress the extraction of iron lattice species but could either slower this process or weaken the stabilization of Mn^{4+} then explaining a lower H/Mn+Fe ratio.

Modifications of redox properties become more apparent when calcium and manganese co-doping are implemented, featured by the broadening of reduction peaks and more distinct separation of the reduction processes as exemplified in Fig. 3(B). Indeed, the reduction of Mn^{4+} to Mn^{3+} shifts towards lower temperature while reduction of Mn^{3+} to Mn^{2+} is delayed as calcium doping content increases. The total hydrogen consumption is boosted on $La_{0.6}Ca_{0.1}Fe_{0.8}Mn_{0.2}O_3$ (1.44 mmol/g) becoming comparable to that measured on $La_{0.7}FeO_3$ (1.45 mmol/g). At a first glance, it could be seen that $La_{0.6}Ca_{0.1}Fe_{0.8}Mn_{0.2}O_3$ mimics the behavior of $La_{0.7}FeO_3$. Nevertheless, a rise in calcium substitution induces lower hydrogen consumption which suggests that calcium substitution would block the extraction/segregation of hematite. Jointly a H_2 consumption process becomes distinguishable above 700°C which intensifies on the stoichiometric $La_{0.6}Ca_{0.4}Fe_{0.8}Mn_{0.2}O_3$ composition emphasizing globally a loss of reducibility assigned either to a lower formation of hematite or a lower stabilization of Mn^{4+}.

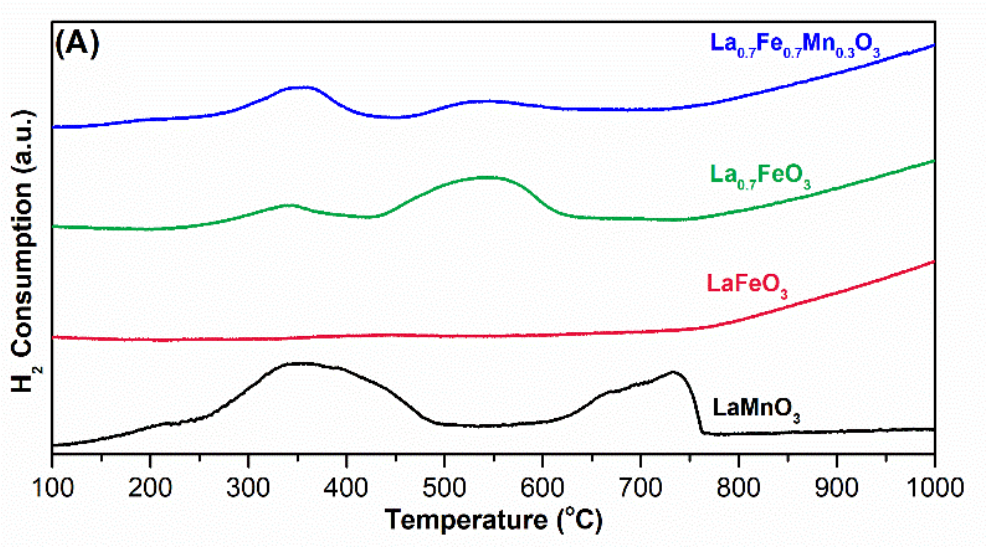

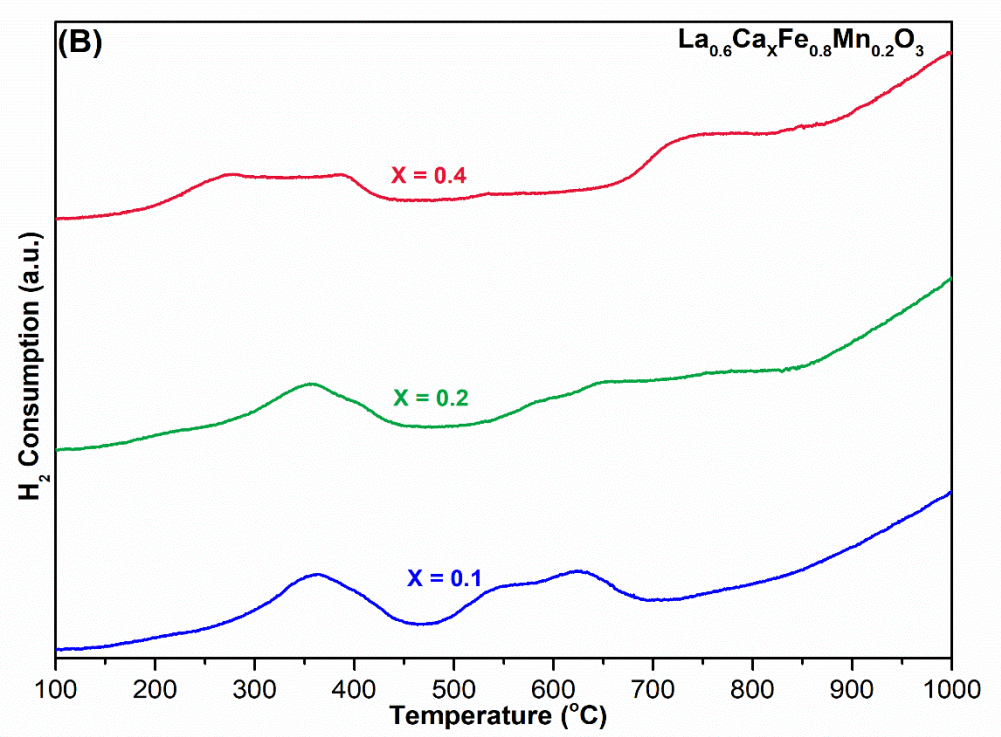

Fig. 3. H_2 consumption curves plotted against temperature on parent stoichiometric $LaFeO_3$ and $LaMnO_3$ compositions and $La_{0.7}Fe_{1-y}Mn_yO_3$ with y = 0 and 0.2 (A) and $La_{0.6}Ca_xFe_{0.8}Mn_{0.2}O_3$ with x = 0.1, 0.2 and 0.4 (B).

3.2.2. Oxygen Temperature Programmed Desorption experiments (O_2-TPD)

O_2-TPD experiments is useful to investigate surface and bulk oxygen mobility. In case of perovskite type materials, two different desorption processes currently appear at low and high

temperature assigned to suprafacial oxygen (α-oxygen) and intrafacial oxygen (β-oxygen) respectively. It was found that α-oxygen desorption would mainly depend on non-stoichiometry and structural defects according to the nature of the A-cations and would correspond to weakly bonded oxygen species [30]. On the other hand, intrafacial oxygen (β-oxygen), desorbing at higher temperature, would be more related to the nature of the B cation and usually ascribed to oxygen lattice species, i.e. O^{2-}. As recently reported [11], α-O_2 desorption can overlap β-O_2 desorption process [31,32] which makes uneasy further assignments and quantification. By way of illustration, Fig. 4 shows a broad α-O_2 desorption on $LaMnO_3$ in the temperature 525-700°C and a faster β-O_2 desorption above 700°C. The former process on $La_{0.7}FeO_3$ is delayed taking place above 650°C and a second desorption process takes place at higher temperature but further assignment can be unclear because of the coexistence of extra-framework iron oxide species. The broad peak appearing more distinctly on $La_{0.7}FeO_3$ below 200°C would correspond to the desorption of weakly bonded hydroxyl species and/or physisorbed oxygen species [33]. This process disappears on single and dual substituted samples. This low temperature desorption process has not been taken into account on the calculation of the total amount of desorbed oxygen. The amount of α-O_2 and β-O_2 released during O_2-TPD has been roughly estimated from the decomposition of the overall signals. Results are reported in Table 4. They essentially reveal a predominant β-O_2 desorption.

The substitution of iron by manganese in $La_{0.7}FeO_3$ leads a much slower desorption of suprafacial oxygen species and a shift to higher temperature of the β-O_2 desorption. Nevertheless, a sharp increase in the amount of oxygen released from the surface is noticeable. Improved bulk oxygen mobility can be rationally explained by the creation of more oxygen vacancies deriving from partial replacement of iron cations by manganese cations. Mössbauer spectroscopic did not reveal the presence of Fe^{4+} induced by A site

deficiency suggesting a charge compensation mostly governed through change in the oxidation state of manganese and/or formation of oxygen vacancies. A slight contraction effect on the cell volume of $La_{0.7}Fe_{0.8}Mn_{0.2}O_3$ would agree with the stabilization of Mn^{4+} exhibiting a lower ionic ratio than Mn^{3+}. Such evolution seems consistent with the desorption features observed on this sample. On the other hand, Fig. 5, illustrating calcium substitution, leads to intriguing observations first related to similar desorption features on $La_{0.6}Ca_{0.1}Fe_{0.8}Mn_{0.2}O_3$ and on $La_{0.7}FeO_3$. An increase in calcium substitution to $x = 0.2$ leads to improved oxygen mobility. The higher amount of desorbed oxygen is consistent with structural changes by considering that more extensive calcium doping should stabilize either iron or manganese cations in B site in higher oxidation state inducing a weakening of the B-O bond. By contrast, the stoichiometric $La_{0.6}Ca_{0.4}Fe_{0.8}Mn_{0.2}O_3$ behaves differently with a sharp loss of oxygen mobility reaching a minimum value of 0.17 mmol/g and seems in reasonable agreement with a loss of reducibility. Hence, despite the beneficial effect of calcium to changes in the valence state of B-cation, the prevalent parameter in determining the extent of oxygen mobility lies in the A-deficiency.

Quantitative analysis of O_2-TPD measurements summarized in Table 4 does not indicate that the specific surface area governs the release of oxygen from the surface. Such observation seems in agreement with the prevalence of an intrafacial oxygen desorption at the expense of suprafacial oxygen desorption.

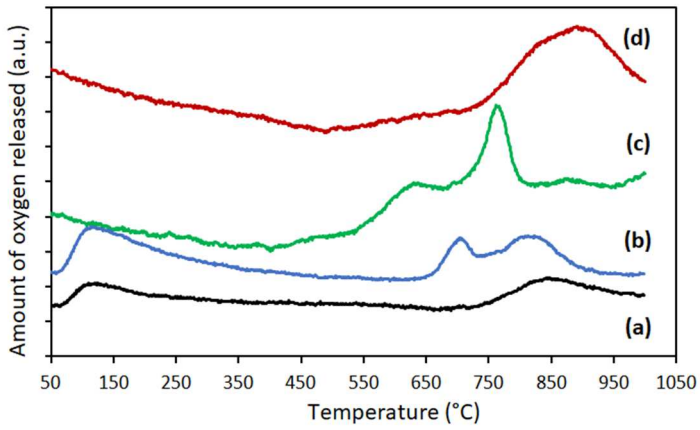

Fig. 4. O_2-TPD profiles recorded on $LaFeO_3$ (a); $La_{0.7}FeO_3$ (b); $LaMnO_3$ (c); $La_{0.7}Fe_{0.8}Mn_{0.2}O_3$ (d).

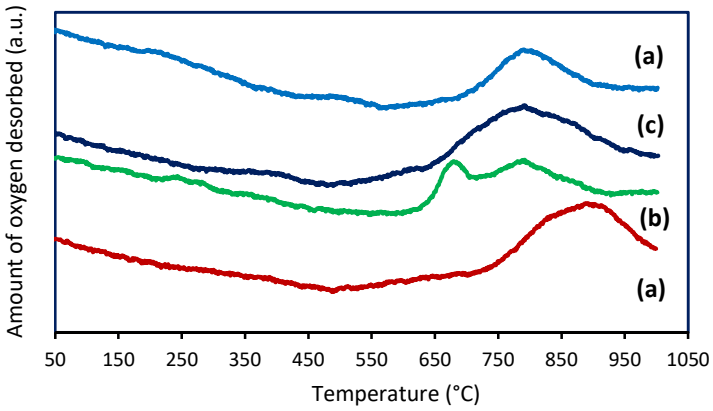

Fig. 5. O_2-TPD profiles recorded on $La_{0.7}Fe_{0.8}Mn_{0.2}O_3$ (a) and $La_{0.6}Ca_xFe_{0.8}Mn_{0.2}O_3$ with x = 0.1 (b); x = 0.2 (c); x = 0.4 (d)

Table 4. Textural properties, reducibility and oxygen desorption features on single and dual substituted parent stoichiometric $LaFeO_3$ and La-deficient $La_{0.7}FeO_3$ perovskite

Catalyst composition	Crystallite size d (nm)[a]	SSA (m^2/g)	S_{th} (m^2/g)[b]	S_{th}/SSA	Pore volume (cm^3/g)	H_2-TPR analysis		O_2 desorbed (mmol/g)	
						H_2 consumption (mmol $^{g-1}$)[c]	H/Fe+Mn	α-O_2 desorption	β-O_2 desorption
$LaFeO_3$	29.4	15.5	30.8	1.99	0.10	-	-	< 0.01	0.03
$La_{0.7}FeO_3$	21.7	35.5	41.7	1.17	0.10	1.45	0.58	0.03	0.09
$LaMnO_3$	38.7	17.8	23.4	1.31	0.09	2.58	1.25	0.05	0.18
$La_{0.7}Fe_{0.8}Mn_{0.2}O_3$	20.4	31.5	44.4	1.41	0.09	1.16	0.47	0.01	0.23
$La_{0.6}Ca_{0.1}Fe_{0.8}Mn_{0.2}O_3$	24.8	32.5	36.5	1.12	0.14	1.44	0.55	0.06	0.14
$La_{0.6}Ca_{0.2}Fe_{0.8}Mn_{0.2}O_3$	23.7	32.6	38.2	1.17	0.13	1.15	0.45	0.04	0.24
$La_{0.6}Ca_{0.4}Fe_{0.8}Mn_{0.2}O_3$	21.3	31.8	42.5	1.34	0.17	0.77	0.31	0.01	0.16

[a] crystallite size from XRD measurements - [b] $S_{th} = 6\times10^3/\rho_{perov.}d$

[c] total H_2 consumption the temperature range 150-700 °C

3.3. Surface properties

3.3.1. Textural properties from nitrogen physisorption

Adsorption isotherms and pore size distribution curves are shown in Fig. S4 in SI. The experimental isotherms of lanthanum ferrite doped with calcium and manganese exhibit a combination of type III and type V isotherms characterized by the absence of B-point at low relative pressure zone yet the presence of hysteresis loop at higher relative pressure zone. The former resulted from the weak interaction between adsorbate and perovskite adsorbent while the latter originated from capillary condensation effect. In all cases, a weak porosity is observable characterized by low pore volume.

Data in Table 4 indicate moderate variations of the specific surface area (SSA) of perovskites doped with manganese in the range of 15.5-35.5 m^2/g. Enlarged SSA combined with decreased crystallites size (see Table 4) manifest improved surface properties. A simple model for depicting the morphology of perovskites and the formation of agglomerates can be used. Such information can be useful to explain their ability to store oxygen. It was earlier explained that oxygen availability can be related to a faster diffusion along the grain boundaries. A rough estimation of theoretical surface S_{th} from the crystallites size can be compared to experimental specific surface area (SSA). As reported elsewhere, the S_{th}-to-SSA ratio can underline the fraction of surface lost by agglomeration between crystal domains as earlier explained [34]. As observed in Table 4, no significant deviation is discernible which emphasizes the fact that changes in SSA are essentially due to the growth of the perovskite crystallites.

3.3.2. Surface composition from XPS analysis

The characteristic La 3d, Fe 2p, Mn 2p and Ca 2p core levels have been examined. The corresponding photopeaks are collected in Figs. S5 and S6 in SI respectively on parent samples, on $La_{0.7}Fe_{0.8}Mn_{0.2}O_3$ and on the series $La_{0.6}Ca_xFe_{0.8}Mn_{0.2}O_3$. Binding energy (BE) near 834 eV on the La 3d photopeak characterizes trivalent cation La^{3+} stabilized inside the perovskite structure. For Ca 2p core level, BE values agree with the stabilization of Ca^{2+}.

The Fe $2p_{3/2}$ photopeak near 710.2 eV, accompanied by a pronounced satellite structure in the range 718-719 eV, is characteristic of Fe^{3+} cations. Mn $2p_{3/2}$ photopeaks exhibit two components assigned to Mn^{3+} (BE = 641.2 eV) and Mn^{4+} (BE = 642.5 eV). [35,36]. Mn 3s photopeak in Fig. S7 in SI provides useful insights on the oxidation state of manganese. Multiplet splitting of Mn 3s peak results from the coupling of non-ionized Mn 3s electrons and 3d valence band electrons [37]. In theory, multiplet splitting can be observed for Mn^{2+}, Mn^{3+} and Mn^{4+} while Mn^{5+} is featured by less defined splitting or broadening. The average oxidation state (AOS) of manganese in the perovskite has been estimated according Eq. (1).

$$\text{Average Oxidation State (AOS)} = 8.956 - 1.12\Delta E_{\text{splitting}}\ (\text{Mn 3s}) \qquad (1)$$

The variation of Mn AOS in perovskite has been closely associated to the nature of A-site and stoichiometry. In general, La-deficiency favors an increase of Mn AOS. To check this assertion spectral features reported on $LaFe_{0.8}Mn_{0.2}O_3$ have been included in Table 5 for further comparison with $La_{0.7}Fe_{0.8}Mn_{0.2}O_3$. This seems in agreement with H_2-TPR showing that La-deficiency can improve the reducibility of the perovskite. Calcium doping with x = 0.1 increases Mn AOS which is supposed to be assigned to the synergistic effect of calcium and manganese. As a matter of fact, the average oxidation state (AOS) of manganese cations for the series $La_{0.6}Ca_xFe_{0.8}Mn_{0.2}O_3$ is mainly determined by the overall cationic charge in A site and continuously decreases reaching a minimum for $La_{0.6}Ca_{0.4}Fe_{0.8}Mn_{0.2}O_3$. It is thereby

assumed that the reducibility of manganese species located in the lattice is affected primarily by the composition of A site. This is supported by a linear increase of the Mn AOS as a function of the total H_2 uptake from H_2-TPR as exemplified in Fig. 6.

Comparison between the O 1s photopeak and the amount of O_2 released from O_2-TPD experiments is not obvious likely due to the predominance of intrafacial β-O_2 desorption. O 1s photopeak is usually characterized by two components ascribed to lattice oxygen species near 529 eV ($O_{lattice}$) and surface O-containing species near 531 eV (O_{ads}). The highest value obtained on $La_{0.7}FeO_3$ is consistent with a low temperature desorption below 250°C. On the other hand, no clear comparison appears with respect to Mn and Ca substitution revealing some discrepancies between the evolution of the values for O_{ads}-to-$O_{lattice}$ ratio with respect to the amount of oxygen released.

Finally, no significant deviation appears by comparing the surface atomic Mn/Fe ratios with those deduce from elemental analysis (see Table S2 in SI) which seems to indicate the absence of preferential segregations of Mn and Fe. Regarding the A/B ratio, some deviations appear distinctly on stoichiometric compositions emphasizing a significant lanthanum surface enrichment.

Table 5. XPS analysis of single and dual substituted calcium manganese $LaFeO_3$ and $La_{0.7}FeO_3$ perovskites

Catalyst	Binding energy (eV)								Semi-quantitative analysis			
	La 3d	Ca 2p	Fe 2p	Mn 2p	$\Delta E_{splitting}$ (eV)	Mn AOS	O 1s (O_{ads})	O 1s ($O_{lattice}$)	Ca/La	Mn/Fe	A/B	$O_{ads}/O_{lattice}$
$LaFeO_3$	833.8	-	710.2	-	-	-	531.1	529.2	-	-	1.34 (1.02)	1.28
$La_{0.7}FeO_3$	834.2	-	710.9	-	-	-	531.2	529.7	-	-	0.48 (0.67)	1.61
$LaFe_{0.8}Mn_{0.2}O_3$	8.34.0	-	710.3	641.7	5.31	2.98	531.5	529.6	-	0.38(0.25)	1.85(0.99)	0.80
$La_{0.7}Fe_{0.8}Mn_{0.2}O_3$	834.1	-	710.5	641.7	5.12	3.19	531.3	529.7	-	0.32 (0.25)	0.67 (0.71)	0.76
$La_{0.6}Ca_{0.1}Fe_{0.8}Mn_{0.2}O_3$	833.9	346.7	710.6	641.8	4.95	3.38	531.4	529.6	0.18 (0.17)	0.32 (0.25)	0.64 (0.68)	0.89
$La_{0.6}Ca_{0.2}Fe_{0.8}Mn_{0.2}O_3$	833.7	346.4	710.2	641.7	5.28	3.01	531.3	529.4	0.31 (0.34)	0.43 (0.25)	0.74 (0.78)	1.10
$La_{0.6}Ca_{0.4}Fe_{0.8}Mn_{0.2}O_3$	833.6	346.4	710.2	641.8	5.62	2.63	531.3	529.0	0.68 (0.38)	0.41 (0.25)	1.27 (1.00)	0.75

Elemental composition in bracket

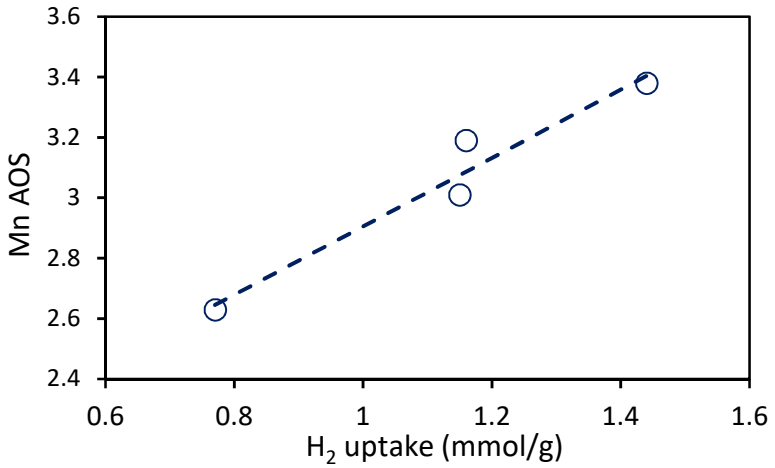

Fig. 6. Comparison between the reducibility and the average oxidation state of manganese (Mn AOS).

3.4. Evaluation of the catalytic properties in three-way conditions

3.4.1. Oxidative properties

Four successive temperature programmed reaction (TPR) experiments were performed in stoichiometric (STO1), lean, rich and stoichiometric (STO2). Prior TPR experiments, the samples were pre-activated in air at 600°C. Conversion profiles vs. temperature for CO, propene and propane oxidation are reported in Fig. 7. STO1 and STOI2 profiles are comparable for CO and propene oxidation underlining the absence of significant deactivation due to surface changes in terms of composition and valence state of active elements. Ca- and Mn-substitutions induce significant gain in conversion compared to the benchmark $La_{0.7}FeO_3$ and $LaFeO_3$ catalysts. La-deficiency has a beneficial effect as well as Mn-substitution. On the other hand, Ca-substitution has no discernible effect for CO oxidation compared to $La_{0.7}Fe_{0.8}Mn_{0.2}O_3$ and a slight detrimental effect is even observed on the rate of propene conversion recorded on the series $La_{0.6}Ca_xFe_{0.8}Mn_{0.2}O_3$. The light-off temperatures collected in Table 6 provide a qualitative overview of the catalytic performances highlighting the superiority of $La_{0.7}Fe_{0.8}Mn_{0.2}O_3$.

Table 6. Light-off temperature (T_{50}) of iron-based perovskite samples.

Catalyst	Light-off temperature T_{50} (°C)					
	STO1			STO2		
	CO	C_3H_6	C_3H_8	CO	C_3H_6	C_3H_8
$LaFeO_3$	480	477	500	487	475	488
$La_{0.7}FeO_3$	395	448	>520	399	456	483
$La_{0.7}Fe_{0.8}Mn_{0.2}O_3$	360	405	518	359	415	514
$La_{0.6}Ca_{0.1}Fe_{0.8}Mn_{0.2}O_3$	366	413	513	369	441	503
$La_{0.6}Ca_{0.2}Fe_{0.8}Mn_{.2}O_3$	375	471	513	388	475	510
$La_{0.6}Ca_{0.4}Fe_{0.8}Mn_{0.2}O_3$	375	462	479	366	458	490

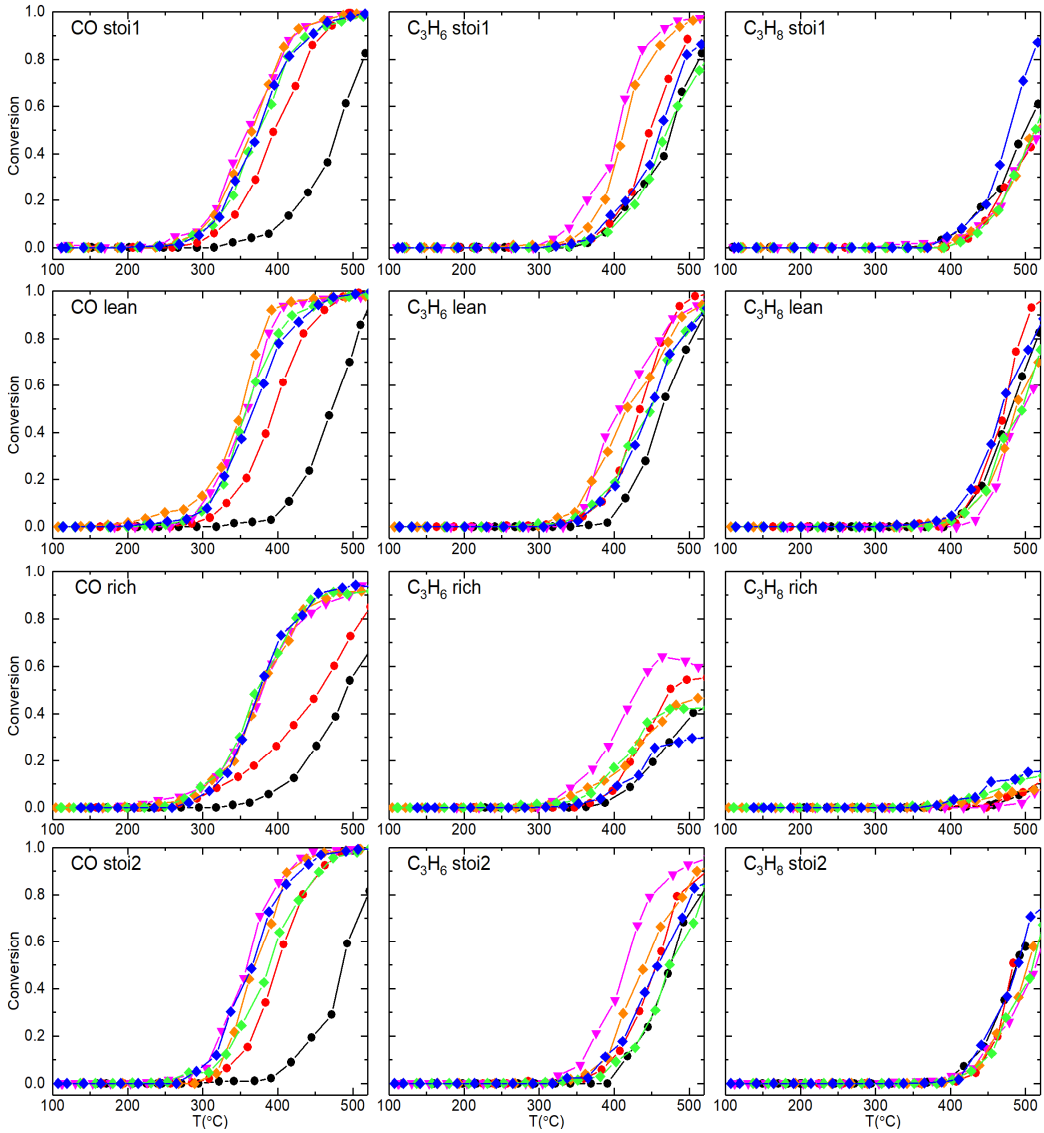

Fig. 7. Catalytic performances of single and dual substituted iron-based perovskites in oxidation reactions : ●$LaFeO_3$; ●$La_{0.7}FeO_3$; ▼ $La_{0.7}Fe_{0.8}Mn_{0.2}O_3$; ◆ $La_{0.6}Ca_{0.1}Fe_{0.8}Mn_{0.2}O_3$; ◆ $La_{0.6}Ca_{0.2}Fe_{0.8}Mn_{0.2}O_3$; ◆ $La_{0.6}Ca_{0.4}Fe_{0.8}Mn_{0.2}O_3$.

Kinetics was analyzed based on Temperature-Programmed CO and propene conversions recorded in stoichiometric conditions at 320°C and 375°C respectively. As described in SI, the mass balance equation of a plug flow reactor and a first order kinetics [38-40] have been assumed for the calculation of the specific and normalized rates, respectively labeled $r_{spec.}$ and r_{norm}. The boundary conditions given by the Weiss-Prater criterion according to Eq. (S4) in SI

was also verified showing the absence of significant perturbations induced by mass transfer phenomena.

Clearly, the evolutions strictly agree with previous tendencies reflecting the highest catalytic properties of $La_{0.7}Fe_{0.8}Mn_{0.2}O_3$ and a detrimental effect of calcium on the reaction rates more accentuated in propene oxidation. The comparison of the pre-exponential factor (A) and apparent activation energy (E_{app}) values of the rate constant k for CO and propene oxidation explain this rate enhancement by a lowering of E_{app}. The pre-exponential factor values in Tables 7 and 8 seem to be independent of the specific surface area and mostly depend on the elemental composition.

Table 7. Impact of single and dual substitution on the kinetic features of $LaFeO_3$ and $La_{0.7}FeO_3$ in CO oxidation.

		STO1				STO2			
Catalyst	S_{BET} (m^2g^{-1})	$r_{spec.}$ [a] (mol s^{-1} g^{-1})	Normalized rate [a] $r_{norm.}$ (mol s^{-1} m^{-2})	A [b] (m^3 s^{-1} g^{-1})	E_{app} [b] (kJ mol^{-1})	$r_{spec.}$ [a] (mol s^{-1} g^{-1})	Normalized rate [a] $r_{norm.}$ (mol s^{-1} m^{-2})	A [b] (m^3 s^{-1} g^{-1})	E_{app} [b] (kJ mol^{-1})
$LaFeO_3$	15.5	0.1×10^{-7}	0.6×10^{-9}	3.6×10^{3}	121.4	0.2×10^{-7}	0.8×10^{-9}	2.9×10^{3}	162.4
$La_{0.7}FeO_3$	35.5	3.4×10^{-7}	9.4×10^{-9}	3.3×10^{3}	107.9	1.8×10^{-7}	5.2×10^{-9}	43.0×10^{3}	123.3
$La_{0.7}Fe_{0.8}Mn_{0.2}O_3$	31.5	7.8×10^{-7}	24.7×10^{-9}	2.0×10^{3}	99.1	7.8×10^{-7}	24.7×10^{-9}	3.6×10^{3}	102.4
$La_{0.6}Ca_{0.1}Fe_{0.8}Mn_{0.2}O_3$	32.5	7.2×10^{-7}	22.3×10^{-9}	3.0×10^{3}	102.2	2.7×10^{-7}	8.3×10^{-9}	3.2×10^{3}	104.3
$La_{0.6}Ca_{0.2}Fe_{0.8}Mn_{0.2}O_3$	32.6	5.6×10^{-7}	17.0×10^{-9}	2.2×10^{3}	102.1	4.0×10^{-7}	12.2×10^{-9}	3.3×10^{3}	106.6
$La_{0.6}Ca_{0.4}Fe_{0.8}Mn_{0.2}O_3$	31.8	5.5×10^{-7}	17.2×10^{-9}	8.2×10^{3}	108.9	5.6×10^{-7}	17.5×10^{-9}	2.9×10^{3}	102.6

[a] calculated at T = 320°C

[b] $k = A \exp(-E_{app}/RT)$

Table 8. Impact of single and dual substitution on the kinetic features of $LaFeO_3$ and $La_{0.7}FeO_3$ in propene oxidation.

		STO1				STO2			
Catalyst	S_{BET} (m^2g^{-1})	$r_{spec.}$ [a] (mol s_{-1} g_{-1})	Normalized rate [a] $r_{norm.}$ (mol s^{-1} m^{-2})	A [b] (m^3 s^{-1} g^{-1})	E_{app} [b] (kJ mol^{-1})	$r_{spec.}$ [a] (mol s^{-1} g^{-1})	Normalized rate [a] $r_{norm.}$ (mol s^{-1} m^{-2})	A [b] (m^3 s^{-1} g^{-1})	E_{app} [b] (kJ mol^{-1})
$LaFeO_3$	15.5	1.1×10^{-8}	6.9×10^{-10}	7.1×10^{3}	125.0	0.8×10^{-8}	5.3×10^{-10}	1.2×10^{4}	129.6
$La_{0.7}FeO_3$	35.5	1.7×10^{-8}	4.88×10^{-10}	7.5×10^{3}	122.6	1.3×10^{-8}	3.6×10^{-10}	4.5×10^{4}	134.0
$La_{0.7}Fe_{0.8}Mn_{0.2}O_3$	31.5	6.7×10^{-8}	21.3×10^{-10}	1.8×10^{3}	106.7	5.6×10^{-8}	17.6×10^{-10}	8.9×10^{3}	117.1
$La_{0.6}Ca_{0.1}Fe_{0.8}Mn_{0.2}O_3$	32.5	4.0×10^{-8}	12.2×10^{-10}	6.6×10^{6}	154.6	2.0×10^{-8}	6.3×10^{-10}	1.7×10^{5}	139.0
$La_{0.6}Ca_{0.2}Fe_{0.8}Mn_{0.2}O_3$	32.6	1.3×10^{-8}	3.9×10^{-10}	6.4×10^{4}	136.0	0.8×10^{-8}	2.4×10^{-10}	4.2×10^{3}	123.0
$La_{0.6}Ca_{0.4}Fe_{0.8}Mn_{0.2}O_3$	31.8	1.8×10^{-8}	5.6×10^{-10}	1.9×10^{3}	115.4	1.0×10^{-8}	3.1×10^{-10}	4.1×10^{5}	145.4

[a] calculated at T = 320°C

[b] $k = A \exp(-E_{app}/RT)$

3.4.2. Reductive properties

NO conversion curves vs. temperature are reported in Fig. 8. NO conversion is weakly detected in lean conditions and slightly improved in stoichiometric conditions on $La_{0.7}Fe_{0.8}Mn_{0.2}O_3$ and $La_{0.6}Ca_{0.1}Fe_{0.8}Mn_{0.2}O_3$. Let us note that for both catalysts, the conversions of propene and CO, in Fig. 7 start nearly at the same temperature than that of NO but conversion curves diverge significantly with a rise in temperature emphasizing the predominant CO and propene oxidation by oxygen. Such observation would agree with a preferential NO reduction by CO at low temperature while at high temperature oxidation reaction by O_2 predominates. By comparing STO1 and STO2, a loss of NO conversion appears more distinctly on $La_{0.6}Ca_{0.1}Fe_{0.8}Mn_{0.2}O_3$. Sharp rate enhancement in NO conversion is observed in rich conditions and still emphasizes the superiority of $La_{0.7}Fe_{0.8}Mn_{0.2}O_3$ compared to $La_{0.6}Ca_xFe_{0.8}Mn_{0.2}O_3$. It is also worthwhile to note a significant NO_x conversion recorded on $La_{0.6}Ca_{0.2}Fe_{0.8}Mn_{0.2}O_3$ in rich conditions while this composition was found inactive in lean and stoichiometric regimes.

By examining the selectivity behavior, no drastic change occurs on $La_{0.7}Fe_{0.8}Mn_{0.2}O_3$ and $La_{0.6}Ca_{0.1}Fe_{0.8}Mn_{0.2}O_3$. Both samples exhibit the same selectivity behavior in lean and stoichiometric conditions (see Fig. 9) with a gradual decrease of N_2O production to the benefit of N_2 vs. temperature. Such changes would not be likely related to the successive N_2O reduction. Indeed, this sub-reaction becomes usually predominant at high NO conversion and would be consequently slower in the residual conversions (being lower than 10%) recorded in our operating conditions. Accordingly, the predominant production of N_2 with a rise in temperature would agree preferentially with a higher activation barrier than that of N_2O formation. In rich conditions, the predominant production of ammonia takes place at high temperature and agrees with fast NO dissociation and simultaneous hydrogenation of adsorbed N atoms by hydrogen instead of N_2 production through the recombination of two

chemisorbed nitrogen atoms. The production of ammonia can be reasonably explained if a source of hydrogen is available. An extra production of H_2 can be originated from reforming or partial oxidation of hydrocarbons in rich conditions. Such hypothesis is supported by the examination of CO conversion profiles vs. temperature in Fig. 7. Indeed, reforming reactions lead to CO as primary product. Accordingly, the sharp loss in CO conversion observed in rich conditions could be reasonably explained by extra CO production through these reactions. Accordingly, a shift from the CO/NO reaction to the NO/H_2 reaction would occur with a rise in temperature in rich conditions likely due to a predominant partial oxidation of propene to CO and H_2 instead of total oxidation.

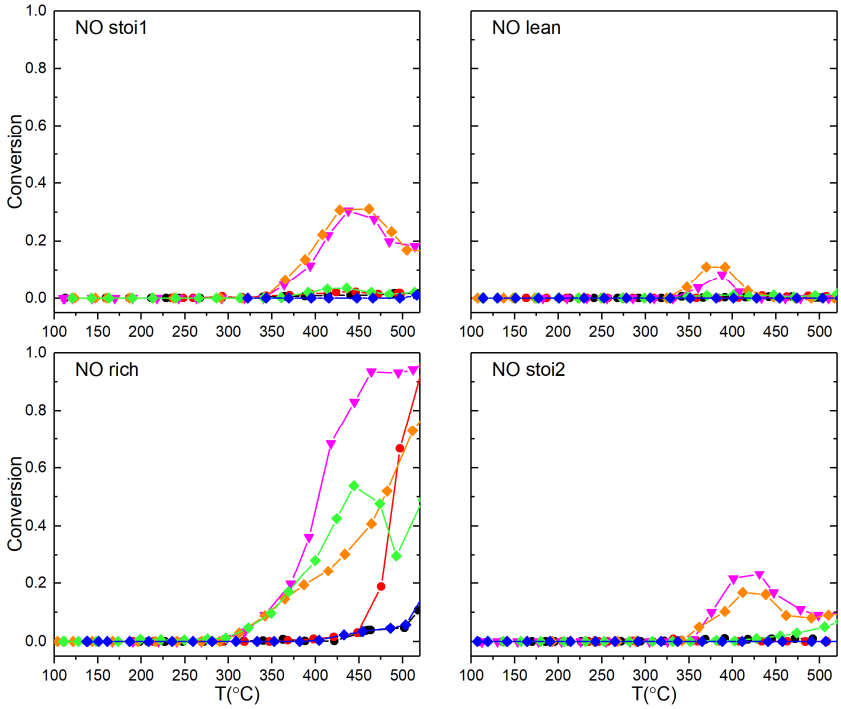

Fig. 8. Catalytic performance of single and dual substituted iron-based perovskites in NO reduction reaction: ● $LaFeO_3$; ● $La_{0.7}FeO_3$; ▼ $La_{0.7}Fe_{0.8}Mn_{0.2}O_3$; ◆ $La_{0.6}Ca_{0.1}Fe_{0.8}Mn_{0.2}O_3$; ◆ $La_{0.6}Ca_{0.2}Fe_{0.8}Mn_{0.2}O_3$; ◆ $La_{0.6}Ca_{0.4}Fe_{0.8}Mn_{0.2}O_3$.

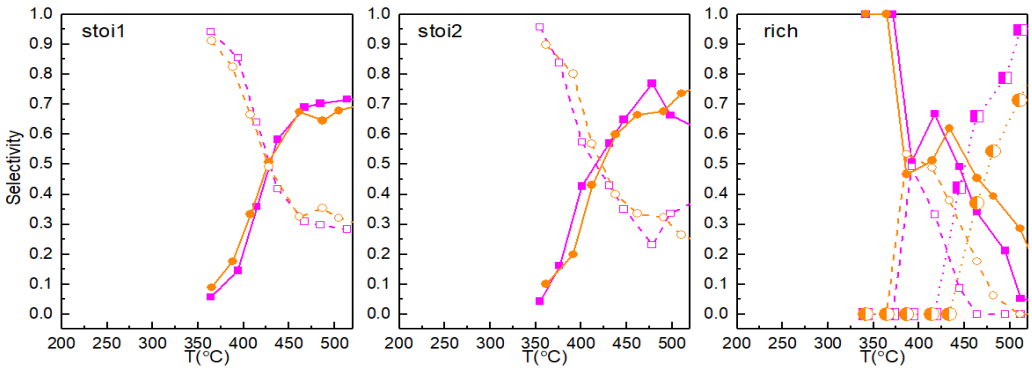

Fig. 9. Selectivity for $La_{0.7}Fe_{0.8}Mn_{0.2}O_3$ (magenta) and $La_{0.6}Ca_{0.1}Fe_{0.8}Mn_{0.2}O_3$ (orange) in stoi1, stoi2 and rich conditions. Magenta solid line solid square $La_{0.7}Fe_{0.8}Mn_{0.2}O_3$ N_2 selectivity (■);Magenta dash line hollow square $La_{0.7}Fe_{0.8}Mn_{0.2}O_3$ N_2O selectivity(□); Magenta dot line big semi-solid square $La_{0.7}Fe_{0.8}Mn_{0.2}O_3$ NH_3 selectivity (◧); Orange solid line solid circle $La_{0.6}Ca_{0.1}Fe_{0.8}Mn_{0.2}O_3$ N_2 selectivity(●); Orange dash line hollow circle $La_{0.6}Ca_{0.1}Fe_{0.8}Mn_{0.2}O_3$ N_2O selectivity(○); Orange dot line big semi-solid circle $La_{0.6}Ca_{0.1}Fe_{0.8}Mn_{0.2}O_3$ NH_3 selectivity(◐).

3.4.3. Discussion on structure-reactivity relationship

The establishment of structure-reactivity relationships for perovskite-type materials is never easy because of the versatility of these materials. Most of the examples dealt with catalytic oxidation reactions. Catalytic properties of perovskite-type materials are governed by the presence of defective sites, which ease adsorption, bulk and surface mobility of oxygen, and the stabilization of cations in unusual valence improving their redox properties. Based on this, two distinct reaction mechanisms can be envisioned. The first one involves lattice oxygen periodically restored at the end of continuous cycles, whereas the second one involves adsorbed gaseous oxygen species and depends on the symmetry of atomic orbitals to be conductive for the reaction [41].

The comparisons on benchmark $LaFeO_3$ and $La_{0.7}FeO_3$ perovskites reveal the beneficial impact of La-deficiency in propene and CO oxidation reactions. An additional gain in activity is clearly observed after substitution of Fe by Mn in $La_{0.7}FeO_3$. By contrast, dual substitution does no longer evidence a synergy effect on the activity in CO and propene conversion. On the contrary Lanthanum substitution by Calcium has a slight detrimental effect on the rate of

CO oxidation which becomes more intense for propene oxidation. Similar trends are observable in STO1 and STO2 series. The weak deviations on the rate values recorded during STO1 and STO2 experiments emphasizes stable surface compositions and the absence of significant alterations of the oxidation state of active elements during lean/rich cycles.

Going back to changes on structural and surface properties induced by single and dual substitutions, clearly calcium substitution provokes sharp structural changes related to contraction of the cell volume at increasing Ca concentration. This contraction effect, more significant for the stoichiometric $La_{0.6}Ca_{0.4}Fe_{0.8}Mn_{0.2}O_3$ composition, has not been related to exsolution and segregation processes but mainly to the stabilization of Fe^{4+}, detected from Mössbauer spectroscopy and characterized by a lower ionic radius than Fe^{3+}. The correlative creation of oxygen vacancies to compensate charge imbalance can accentuate this contraction effect. Similarly, the stabilization of Mn^{4+} at the expense of Mn^{3+}, characterized by a lower ionic radius (0.56 Å vs. 0.66 Å for Mn^{3+}) can equally explained these contraction effects. Such hypotheses have been previously envisioned by Onrubia et al. [1] who privileged an increase of the oxidation state of manganese rather than formation of anionic vacancies for explaining the better catalytic properties of Sr-doped perovskites in NO reduction. Clearly, our results differ from those obtained by these authors because La^{3+} substitution by Ca^{2+} leads to lower rates in NO conversion, the most active sample being $La_{0.7}Fe_{0.8}Mn_{0.2}O_3$.

H_2-TPR and O_2-TPD measurements are bulk sensitive characterizing the reducibility and oxygen mobility. No reliable comparison can be drawn with rate values in Table 9. Quantitative comparisons between H_2 uptake from H_2-TPR experiments and the amount of O_2 release from desorption according to the degree of substitution is not obvious. Interestingly, H_2 uptake diminishes at increasing Ca doping which could contradict a greater formation of Mn^{4+}. In practice we demonstrate that calcium also blocks the formation of more reducible hematite promoted on La-deficient perovskite samples. Regarding O_2-TPD experiments, O_2

desorption is promoted on La-deficient perovskites more prone to form anionic vacancies and occurs more readily on $La_{0.6}Ca_xFe_{0.8}Mn_{0.2}O_3$ with x = 0.1 and 0.2 at lower temperature. On the other hand, opposite trends are observed on the stoichiometric $La_{0.6}Ca_{0.4}Fe_{0.8}Mn_{0.2}O_3$ composition. Nakamura et. al [42] proposed on $La_{1-x}Sr_xCoO_{3-\delta}$ that increasing the perovskites reducibility decreases its propensity to refill its oxygen vacancies. This suggests that a poorer activity could be expected in case of intrafacial mechanism. Obviously, neither the bulk reducibility of the B cation nor the bulk oxygen mobility would act as critical parameters based on the comparison of H_2 uptake and oxygen release for explaining the impact of single and dual substitutions on the catalytic properties. The absence of correlation between catalytic properties and bulk physicochemical properties has been already pointed out on $LaCo_{1-x}Fe_xO_3$ [35] for the methane oxidation reaction preferentially obeying to a suprafacial mechanism. Nevertheless, the comparison of rate values with specific surface area is also unable to explain the trends observed of the catalytic properties. Indeed, the rates as well as the pre-exponential factor values of the rate constant vary independently with the specific surface area emphasizing the primacy of the surface composition and oxidation state of active elements. Both parameters would act as critical parameters in determining the catalytst properties. Nevertheless, an important question arises related to the involvement of the mixed oxidation states Fe^{4+}/Fe^{3+} and Mn^{4+}/Mn^{3+} in particular the one that will prevail.

Tables 9 compares kinetic data with physicochemical properties. An important information comes from the comparison of $La_{0.7}FeO_3$ and $LaFeO_3$ in CO oxidation which clearly demonstrates that the rate enhancement observed on the former composition cannot be formally explained by the presence of Fe^{4+} in the bulk and/or at the surface. Such tendency persists for propene oxidation but in lesser extent. Based on this, any participation of Fe(+IV) as active species can be ruled out in the oxidative properties of Ca-doped samples. Subsequent, rate improvements on $La_{0.7}Fe_{0.8}Mn_{0.2}O_3$ both for oxidation and reduction

reactions emphasize the prevalent role of high oxidation state of manganese corresponding to higher rates and lower activation barriers for CO and propene oxidation. Mössbauer spectroscopy did not detect for this sample the presence of Fe^{4+} which seems in relative agreement with previous investigation reported by Leontiou et al. [11] who observed that the highest activity in NO reduction by CO correspond to the lowest amount of Fe^{4+} and the highest amount of Fe^{3+}.

As found, Ca substitution leads to lower rates explained by an increase in E_{app}. Correlatively, a significant decrease in the manganese average oxidation state is noticeable with a predominant stabilization of Mn(+III). Such a tendency could be responsible for the slight increase observed in Mn/Fe surface composition. Accordingly, a slight aggregation/segregation of small clusters of Mn_2O_3 or MnO cannot be excluded. Alternately, this evolution on the relative surface concentration of manganese could be related to lower extent of hematite segregation. This is due to the stabilizing effect of calcium maintaining iron stabilized as Fe^{4+} in octahedral position of the perovskite. Such changes in physicochemical properties could rationally explain the loss of catalytic properties due to calcium substitution especially for the stoichiometric $La_{0.6}Ca_{0.4}Fe_{0.8}Mn_{0.2}O_3$ compositions.

To summarize, A-site deficiency coupled to manganese doping in B site results in better reducibility of lanthanum ferrite that could create more oxygen vacancies essential for the adsorption of NO and O_2 in competition. In parallel, a cooperation between iron and manganese is suggested for the stabilization of Mn^{4+} at the vicinity of anionic vacancies. Clearly, Ca doping has a detrimental impact because electronic imbalance would be more compensated by an increase of the oxidation state of Fe^{3+} to Fe^{4+} as observed from Mössbauer spectroscopy. This could explain the smallest $O_{ads}/O_{lattice}$ ratio for the stoichiometric composition $La_{0.6}Ca_{0.4}Fe_{0.8}Mn_{0.2}O_3$. Hence, low anionic vacancies jointly with low Mn AOS

can reasonably explain the low catalytic performance of this catalyst both for oxidation and reduction reaction.

Table 9. Comparison between physicochemical and catalytic properties for CO and propene oxidation

Catalysts	S_{BET} (m^2 g^{-1})	Unit cell volume (Å^3)	Fe^{4+}/Fe^{3+}	H_2 uptake (mmol/g)	O_2 desorbed (mmol/g)	Mn AOS	$O_{ads}/O_{latt.}$	Mn/Fe	STO1			STO2		
									$r_{spec.}$ (mol s^{-1} g^{-1})	A (m^3 s^{-1} g^{-1})	E_{app} (kj mol^{-1})	$r_{spec.}$ (mol s^{-1} g^{-1})	A (m^3 s^{-1} g^{-1})	E_{app} (kj mol^{-1})
CO oxidation														
$LaFeO_3$	15.5	242.88	4.83	0	0.04		1.28		0.2×10^{-7}	3.6×10^{3}	121.4	0.2×10^{-7}	2.9×10^{3}	162.4
$La_{0.7}FeO_3$	35.5	242.44	0	1.45	0.14		1.61		1.8×10^{-7}	3.3×10^{3}	107.9	1.8×10^{-7}	43.0×10^{3}	123.3
$La_{0.7}Fe_{0.8}Mn_{0.2}O_3$	31.5	240.07	0	1.16	0.23	3.19	0.76	0.32	7.8×10^{-7}	2.0×10^{3}	99.1	7.8×10^{-7}	3.6×10^{3}	102.4
$La_{0.6}Ca_{0.1}Fe_{0.8}Mn_{0.2}O_3$	32.5	238.22	3.99	1.44	0.23	3.38	0.89	0.32	2.7×10^{-7}	3.0×10^{3}	102.2	2.7×10^{-7}	3.2×10^{3}	104.3
$La_{0.6}Ca_{0.2}Fe_{0.8}Mn_{0.2}O_3$	32.6	237.46	3.35	1.15	0.33	3.01	1.10	0.43	4.0×10^{-7}	2.2×10^{3}	102.1	4.0×10^{-7}	3.3×10^{3}	106.6
$La_{0.6}Ca_{0.4}Fe_{0.8}Mn_{0.2}O_3$	31.8	233.78	2.72	0.77	0.16	2.63	0.75	0.41	5.6×10^{-7}	8.2×10^{3}	108.9	5.6×10^{-7}	2.9×10^{3}	102.6
Propene oxidation														
$LaFeO_3$	15.5	242.88	4.83	0	0.04		1.28		1.1×10^{-8}	7.1×10^{3}	125.0	0.8×10^{-8}	1.2×10^{4}	129.6
$La_{0.7}FeO_3$	35.5	242.44	0	1.45	0.14		1.61		1.7×10^{-8}	7.5×10^{3}	122.6	1.3×10^{-8}	4.5×10^{4}	134.0
$La_{0.7}Fe_{0.8}Mn_{0.2}O_3$	31.5	240.07	0	1.16	0.23	3.19	0.76	0.32	6.7×10^{-8}	1.8×10^{3}	106.7	5.6×10^{-8}	8.9×10^{3}	117.1
$La_{0.6}Ca_{0.1}Fe_{0.8}Mn_{0.2}O_3$	32.5	238.22	3.99	1.44	0.23	3.38	0.89	0.32	4.0×10^{-8}	6.6×10^{6}	154.6	2.0×10^{-8}	1.7×10^{5}	139.0
$La_{0.6}Ca_{0.2}Fe_{0.8}Mn_{0.2}O_3$	32.6	237.46	3.35	1.15	0.33	3.01	1.10	0.43	1.3×10^{-8}	6.4×10^{4}	136.0	0.8×10^{-8}	4.2×10^{3}	123.0
$La_{0.6}Ca_{0.4}Fe_{0.8}Mn_{0.2}O_3$	31.8	233.78	2.72	0.77	0.16	2.63	0.75	0.41	1.8×10^{-8}	1.9×10^{3}	115.4	1.0×10^{-8}	4.1×10^{5}	145.4

4. Conclusion

Lanthanum ferrite perovskite with orthorhombic structure was prepared by conventional citric method. Such crystal structure was preserved after partial substitution in A- or B-site. Parent $LaFeO_3$ and $La_{0.7}FeO_3$ perovskites reveal that La-deficiency promotes the formation of extra-framework hematite species. Mn doping in B-site of La-deficient $La_{0.7}FeO_3$ perovskite did not result in significant phase segregation irrespective to Mn doping degree or A-site composition. By contrast, contraction of unit cell volume and significant structural distortions characterized from Mössbauer spectroscopy appear especially on the stoichiometric $La_{0.6}Ca_{0.4}Fe_{0.8}Mn_{0.2}O_3$ composition. The stabilization of Fe^{4+} proceeds on stoichiometric composition and improves with partial substitution of La by Ca in A-site. Average oxidation state (AOS) of doped Mn species also depends heavily on A-site composition. It is noticeable that Mn^{4+}/Mn^{3+} ratio changes according to the elemental composition of the solid and that La-deficiency favors an increase of Mn^{4+}/Mn^{3+} ratio. By contrast, a rise in Ca content decreases the Mn^{4+}/Mn^{3+}.

With regard to oxidative properties and reductive properties, $La_{0.7}Fe_{0.8}Mn_{0.2}O_3$ represents the best formulation with enhanced reaction rates associated with lower apparent activation energy values. Minor deviation between STO1 and STO2 underlines the high stability of the surface properties with no obvious segregation after lean/rich cycle. As general trend, the catalytic activity is not governed by the extent of surface area but mostly by the surface composition, ie. the valence of manganese and the La-deficiency. Subsequent Ca-substitution induces a detrimental effect on the oxidation and reduction reaction rates reasonably explained by a decrease of the oxidation state of manganese. Jointly, the formation of Fe^{4+} is still detected emphasizing the fact that the redox properties are rather governed by the Mn^{4+}/Mn^{3+} couple than Fe^{4+}/Fe^{3+} couple.

Despite, the reduction of NO is slow, it clearly appears that the CO/NO reaction predominates at low temperature. On the other hand, the NO/H_2 reaction prevails at high temperature especially in rich conditions when an extra production of hydrogen from partial oxidation and reforming reactions of propene and propane take place predominantly. The involvement of such sub-reactions has a detrimental impact on the selectivity towards N_2 production with a significant production of ammonia.

Acknowledgements

The authors would like to thank the EU-Partial-PGMs project (H2020-NMP-686086) for financial support. Chevreul Institute (FR 2638), Ministère de l'Enseignement Supérieur et de la Recherche, Région Nord – Pas de Calais and FEDER are also acknowledged for supporting partially this work. We also thank Martine Trentesaux and Pardis Simon who conducted XPS measurements and Olivier Gardoll for thermal analysis.

Reference

1. J.A. Onrubia, B. Pereda-Ayo, U. De-La-Torre, J.R. González-Velasco, Appl. Catal. B 213 (2017) 198–210.
2. C.H. Kim, G. Qi, K. Dahlberg, W. Li, Science 327 (2010) 1624–1627.
3. A. Russell, W.S. Epling, Catal. Rev. 53 (2011) 337–423.
4. N. Russo, D. Fino, G. Saracco, V. Specchia, J Catal. 229 (2005) 459–469.
5. J. Chen, M. Shen, X. Wang, G. Qi, J. Wang, W. Li, Appl. Catal. B 134–135 (2013) 251–257.
6. R. Spinicci, A. Delmastro, S. Ronchetti, A. Tofanari. Mater. Chem. Phys. 78 (2002) 393–399.
7. M. Alifanti, G. Bueno, V. Parvulescu, V.I. Parvulescu , V. Cortés Corberán, Catal. Today 143 (2009) 309–314.
8. V. Roche, R. Revel, P. Vernoux, Catal. Comm. 11 (2010) 1076–1080.
9. J. Zhang, D. Tan, Q. Meng, X. Weng, Z. Wu. Appl. Catal. B 172–173 (2015) 18–26.
10. J. Wu, J.P. Dacquin, C. Cordier, C. Dujardin, P. Granger, Appl. Catal. B 282 (2021) 119621.
11. A.A. Leontiou, A.K. Ladavos, P.J. Pomonis. Appl. Catal. A 241 (2003) 133–141.
12. J. Zhu, A. Thomas. Appl. Catal. B 92 (2009) 225–233.
13. B. Kucharczyk, W. Tylus, Appl. Catal. A 335 (2008) 28–36.
14. S. Cimino, L. Lisi, S. De Rossi, M. Faticanti, P. Porta. Appl. Catal. B 43 (2003) 397–406.
15. R. Zhang, A. Villanueva, H. Alamdari, S. Kaliaguine. Appl. Catal. B 64 (2006) 220–233.
16. R. Zhang, A. Villanueva, H. Alamdari, S. Kaliaguine. Appl. Catal. A 307 (2006) 85–97.
17. R. Zhang, A. Villanueva, H. Alamdari, S. Kaliaguine. J. Mol. Catal. A 258 (2006) 22–34.
18. H. Tanaka, N. Mizuno, M. Misono. Appl. Catal. A 244 (2003) 371–382.

19. H. Taguchi, S. Matsu-ura, M. Nagao. J. Solid State Chem. 129 (1997) 60–65.
20. L. Ortega-San Martin, J.P. Chapman, E. Hernandez-Bocanegra, M. Onsauti, M.I. Arriortua, J. Phys. Condens. Matter 16 (2004) 3879–3888.
21. A.K. Eriksson, S.-G. Eriksson, S.A. Ivanov, C.S. Knee, J. Eriksen, H. Rundlöff , M. Tseggai. Mater. Res. Bull. 41 (2006) 144–157.
22. J.-H. Choy, J.H. Park, S.-T. Hong, D.-K. Kim. J. Solid State Chem. 111 (1994) 370–379.
23. J.-H. Choy, S.-T. Hong, K.-S. Choi, J. Chem. Soc. Faraday Trans. 92 (1996) 1051–1059.
24. Y. Wu, C. Cordier, E. Berrier, N. Nuns, C. Dujardin, P. Granger, Appl. Catal. B 140-141 (2013) 151–153.
25. K. Świerczek, J. Marzec, D. Pałubia, K.W. Zając, J. Molenda, Solid State Ionics, 177 (2006) 1811–1817.
26. T. Hernandez, F. Plazaola, T. Rojo, J.M. Barandiaran, J. Alloys Compounds 323–324 (2001) 440–443.
27. L.C.A. Oliveira, J.D. Fabris, R.R.V.A. Rios, W.N. Mussel, R.M. Lago, Appl. Catal. A 259 (2004) 253–259.
28. D. Varshney, A. Yogi, Mater. Chem. Phys. 128 (2011) 489–494.
29. U. Russo L. Nodari, M. Faticanti, V. Kuncser, G. Filoti, Solid State Ionic 176 (2005) 97–102.
30. L.G. Tejuca, J.L.G. Fierro, J.M.D. Tascón, Adv. Catal. 36 (1989) 237–328.
31. B. Levasseur, S. Kaliaguine, Appl. Catal. B 88 (2009) 305–314.
32. Y. Wu, L. Li, B. Bhu, Y. Li, Z. Qin, M. Fan, Q. Qin, H. He, L. Zhang, L. Dong, B. Li, L. Dong, Appl. Catal. A 568 (2018) 43–53.
33. N.A. Merino, B.P. Barbaro, P. Grange, L.E. Cadús, J. Catal. 231 (2005) 232-244.
34. S. Royer, F. Bérubé, S. Kaliaguine. Appl. Catal. A 282 (2005) 273–284.
35. H.W. Nesbitt, D. Banerjee, American Mineralogist, 83 (1998) 305–315.
36. D. Banerjee, H.W. Nesbitt. Geochimica et Cosmochimica Acta 63 (1999) 3025–3038.
37. H. Najjar, J.-F. Lamonier, O. Mentré, J.M. Giraudon, H. Batis, Catal. Sci. Technol. 3 (2013) 1002–1016.
38. A. Schön, C. Dujardin, J.P. Dacquin, P. Granger. Catal. Today 258 (2015) 543–548.
39. J.L. Hueso, D. Martínez-Martínez, A. Caballero, A.R. González-Elipe, B.S. Mun, M. Salmerón, Catal. Commun. 10 (2009) 1898–1902.
40. G. Parravano. J. Am. Chem. Soc. 75 (1953) 1497–1498.
41. R.J.H. Voorhoeve in Advance Materials in Catalysis, Eds. J.J. Burton, R.L. Garten, Academic press, New York, 1977, p. 129.
42. T. Nakamura, M. Misono, Y. Yoneda, J. Catal. 83 (1983) 151–159.

Graphical Abstract